Available online at www.sciencedirect.com
ScienceDirect
Combustion and Flame 155 (2008) 37–53
Combustion and Flame
www.elsevier.com/locate/combustflame

Extinguishment of methane diffusion flames by carbon dioxide in coflow air and oxygen-enriched microgravity environments

Fumiaki Takahashi [a,*], Gregory T. Linteris [b], Viswanath R. Katta [c]

[a] *National Center for Space Exploration Research on Fluids and Combustion, NASA Glenn Research Center, 21000 Brookpark Road, Cleveland, OH 44135, USA*
[b] *Fire Research Division, National Institute of Standards and Technology, 100 Bureau Drive, Gaithersburg, MD 20899, USA*
[c] *Innovative Scientific Solutions Inc., 2766 Indian Ripple Road, Dayton, OH 45440, USA*

Received 18 October 2007; received in revised form 14 February 2008; accepted 10 March 2008

Available online 30 April 2008

Abstract

Microgravity experiments and computations have been conducted to elucidate stabilization and extinguishment mechanisms of methane diffusion flames, in the cup-burner configuration, with CO_2 added gradually to a coflowing air or oxygen-enriched stream. The minimum extinguishing concentration of CO_2 under low oxidizer velocities (<20 cm/s) was measured in microgravity achieved by parabolic flights of the NASA Reduced Gravity Aircraft. Transient computations with full chemistry and a gray-gas radiation model were performed to reveal the detailed flame structure and extinguishment processes. To compensate for the overestimation of radiative heat losses at high concentrations of radiating CO_2, the Planck mean absorption coefficient was multiplied by a correction factor ($0 \leqslant C \leqslant 1$). The fuel-lean peak reactivity spot (the so-called reaction kernel) at the flame base stabilized the trailing diffusion flame. The calculated temperature along the trailing flame decreased downstream due to radiative cooling, leading to local extinction at <1300 K and flame tip opening. As CO_2 was added to the oxidizer: (1) the calculated maximum flame temperature decreased toward a threshold (≈1600 K); (2) the reaction kernel weakened (i.e., lower heat release rate) but nonetheless remained at a nearly constant temperature (≈1450 K); (3) the flame base stabilized increasingly higher above the burner rim, parallel to the axis; until finally, (4) blowoff-type extinguishment occurred. In the lifted flame, the broadened reaction kernel supported a super-lean reaction branch on the oxidizer side as well as the trailing diffusion flame on the fuel-rich side (no triple flame structure was formed).

Keywords: Diffusion flame stabilization; Spacecraft fire suppression; Carbon dioxide; Reaction kernel; Microgravity

1. Introduction

Fire safety for spacecraft and planetary surface bases is essential for mission success in human exploration of space [1–3]. Spacecraft have been equipped with fire extinguishers as protection against spread-

* Corresponding author. Fax: +1 216 433 3793.
E-mail address: fxt13@case.edu (F. Takahashi).

0010-2180/$ – see front matter
doi:10.1016/j.combustflame.2008.03.005

ing fires. The Space Shuttle has extinguishers charged with Halon 1301 (CF_3Br, bromotrifluoromethane); however, Halon production has been banned by the Montreal Protocol [4] because of its high ozone-depletion potential, in spite of its high effectiveness as a fire-extinguishing agent. The International Space Station (ISS) has portable extinguishers charged with gaseous carbon dioxide (CO_2) in the U.S. module, and water-based foam in the Russian module. The thermally acting agent carbon dioxide (CO_2), selected through tradeoff studies [5,6], has advantages in its low cost, availability, reliability, and absence of halogenated decomposition products. It is, however, relatively inefficient compared to chemically active agents [7,8], and leakage of CO_2 can create a toxic atmosphere [9]. In terrestrial applications, new installations of total flooding fire-extinguishing systems employing CO_2 are prohibited in normally occupied spaces under most circumstances [10]. Water-based foams have certain advantages, yet postfire cleanup of residues may become a problem. Although the current systems in spacecraft will continue to be used, upcoming long-duration space missions [11] seek alternatives. While water is an effective fire-extinguishing agent, CO_2 is of particular interest for use on the martian surface base because it is a major component of that planet's atmosphere (95.3% CO_2 at 0.6–1.5 kPa total pressure [2]) and will likely be available from in situ resources utilization processes.

Fire suppression becomes more difficult as the oxygen concentration increases [12–14]. The worst-case oxygen concentration and pressure condition in current, nominally operating spacecraft is 30% O_2 in N_2 at 70.3 kPa [2]. This atmosphere corresponds to the Shuttle and ISS environments that are prescribed for crew conditioning prior to extravehicular activities (EVA). Even higher oxygen concentrations at reduced pressures could possibly be used in space exploration in the future [15]. The fire suppression behavior and the effectiveness of fire-extinguishing agents in high-oxygen-concentration reduced-pressure microgravity environments have not yet been fully studied. Qiao et al. [16] determined the effects of chemically passive agents on the burning velocity of premixed flames under the pre-EVA microgravity conditions, and Shebl et al. [17] studied their effects on the extinction of counterflow diffusion flames.

As a result of significant progresses in the development of detailed combustion reaction mechanisms and computer technologies over the past two decades, it is now feasible to simulate various transient combustion phenomena in simple configurations (burner geometry, flow, and fuel) with reasonable accuracy. The authors have reported the experimental and computational results of the stabilization mechanisms of laminar hydrocarbon jet diffusion flames [18–21] and the extinguishment of coflow methane diffusion flames by various agents [22–29], in the cup burner configuration [30,31], at normal earth gravity ($1g_n$) and microgravity (μg). The predicted minimum extinguishing concentration (MEC) of each agent was generally in good agreement (typically within less than $\pm 10\%$) with the measurement. At μg, because of smaller heat-release rates and generally longer residence times, the radiative heat loss becomes more significant than it is at $1g_n$. It has been reported [32,33] that the gray-gas radiation model overpredicts radiative loss. This trend becomes particularly evident when CO_2 is added at high concentrations to oxygen-enriched environments (which have higher flame temperatures).

The overall objectives of the present study are to understand the physical and chemical processes of diffusion flame stabilization and extinguishment phenomena and to provide rigorous testing of numerical models, which include detailed chemistry and radiation submodels. This paper extends the previous work [22,23] on cup-burner flame suppression using CO_2, reporting new μg results from tests in the NASA Reduced-Gravity Aircraft, including data at higher oxygen volume fraction in the oxidizer ($X_{O_2,ox}$), together with computations employing improved treatment of the radiative heat loss.

2. Experimental procedures

Fig. 1 shows the experimental apparatus aboard the NASA Reduced Gravity Aircraft (KC-135 or C-9B), which consists of an experiment control system and a cylindrical test chamber (25.5-cm inner diameter × 53.3-cm length) containing a cup burner apparatus. A cylindrical stainless-steel cup (28-mm i.d., 31-mm o.d., 45° chamfered inside the rim) is positioned coaxially inside a quartz chimney (85-mm i.d., 45.7-cm height), through which the oxidizer with fire-extinguishing agent (CO_2) flows. The burner surface temperature was measured at 0.5 mm from the burner tip using a K-type thermocouple (Omega CO2-K, 0.254-mm wire diameter). The burner was heated with an electric disc heater (43 W) placed underneath the fuel cup to keep its temperature from dropping below 100 °C prior to ignition and after extinguishment.

To provide uniform flow, a perforated distribution tube, two layers of perforated plates, two layers of honeycomb plates, and two stainless-steel mesh screens atop the honeycomb are placed in the base of the chimney. In addition, two layers of perforated plates and three mesh screens are placed in the fuel cup. The exhaust from the test chamber is connected to an aircraft overboard vent via a back-pressure reg-

(a)

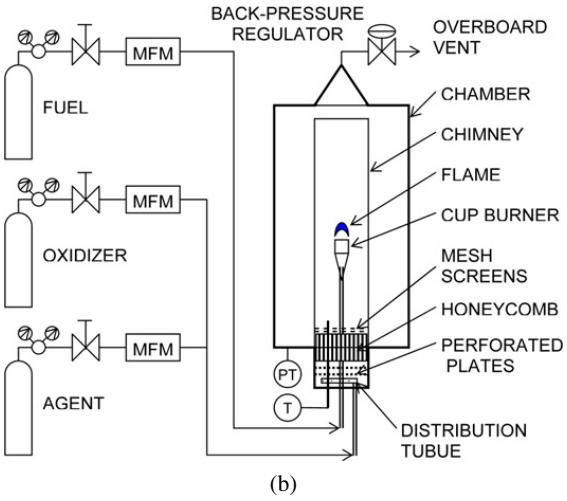

(b)

Fig. 1. The NASA Reduced-Gravity Aircraft fire-suppression rig used. (a) Photograph, (b) flow system.

ulator (Tescom, 44-4700, ER3000[1]), which maintains the chamber at a set pressure. Gas flow rates were measured by mass flow meters (Hastings HFM-300/301), which were calibrated so that their uncertainty is 1% of indicated flow. The fuel is methane (Matheson UHP, 99.97%), the agent is CO_2 (Airgas, 99.99%), and the oxidizer is an O_2–N_2 mixture (O_2 concentration in volume: $[21 \pm 0.2]$% or $[30 \pm 0.3]$%; AGA, primary standard).

The experimental control and data acquisition were achieved by using a computer (Pentium M, 1.4 GHz) with LabVIEW software. The flame radiation was measured by a radiometer (Dexter, ST150 amplified, nitrogen-filled, KRS-5 window) with a neutral density filter, placed with its optical axis perpendicular to the burner axis. The flame was ignited by a hot-wire igniter (coiled 29-gauge Kanthal) during the high-g (approx. $1.8g_n$; g_n is normal earth gravity, 9.8 m/s^2) pull-up period. To determine the extinguishing condition, the agent was introduced to the coflowing oxidizer after the low-g condition was attained and added incrementally, while maintaining constant methane and oxidizer flow rates. Reported uncertainties in the experimental data are of Type B, expressed as expanded uncertainties, with a coverage factor of 2. The uncertainty in the MEC is 3.4%, in gas coflow velocity 3.6%, and test chamber pressure 1%.

[1] Certain commercial equipment, instruments, or materials are identified in this paper to adequately specify the procedure. Such identification does not imply recommendation or endorsement by NASA or NIST, nor does it imply that the materials or equipment are necessarily the best available for the intended use.

3. Computational methods

A time-dependent, axisymmetric numerical code (UNICORN) [34,35] is used for the simulation of coflow diffusion flames stabilized on the cup burner. The code solves the axial and radial (z and r) full Navier–Stokes momentum, enthalpy- and species-conservation, and continuity equations on a staggered-grid system. The body-force term due to the gravitational field is included in the axial-momentum equation to simulate upward-oriented flames in $1g_n$. A clustered mesh system is employed to trace the gradients in flow variables near the flame surface. A detailed reaction mechanism of GRI-V1.2 [36] for methane–oxygen combustion (31 species and 346 elementary reactions) is incorporated into UNICORN. Thermophysical properties of species are calculated from the polynomial curve fits for 300–5000 K. Mixture viscosity and thermal conductivity are then estimated using the Wilke and Kee expressions [37], respectively.

A simple radiative heat-loss model [38] based on optically thin media and gray-gas assumptions was incorporated into the energy equation. To compensate for overprediction of radiative loss, the mean absorption coefficient was multiplied by a correction factor ($0 \leqslant C \leqslant 1$). The radiative loss rate per unit volume is calculated as

$$Q_r = C\sigma \sum_i \{p_i a_{p,i}\}\left(T^4 - T_b^4\right), \tag{1}$$

where σ is the Stefan–Boltzmann constant (5.669×10^{-8} W/m^2 K^4), summation is over the species CO_2, H_2O, CH_4, and CO, p_i is the partial pressure of species i in atmospheres, $a_{p,i}$ is the Planck mean absorption coefficient of species i, T is the local temperature (K), and T_b is the background temperature (294 K).

The finite-difference forms of the momentum equations are obtained using an implicit QUICKEST scheme [34], and those of the species and energy

equations are obtained using a hybrid scheme of upwind and central differencing. At every time step, the pressure field is accurately calculated by solving all the pressure Poisson equations simultaneously and using the LU (lower and upper diagonal) matrix-decomposition technique.

Unsteady axisymmetric calculations for the cup-burner flames are made on a physical domain of 200 by 47.5 mm using a 251 × 101, 541 × 251, or 991 × 251 nonuniform grid system that yielded 0.2 by 0.2 mm (for the first) or 0.05 by 0.05 mm (for the latter two) minimum grid spacing in both the z and r directions in the flame zone. The latter grid systems were used to refine the distributions of the variables calculated with the first. The computational domain is bounded by the axis of symmetry and a chimney wall boundary in the radial direction and by the inflow and outflow boundaries in the axial direction. The outflow boundary in z direction is located sufficiently far from the burner exit (∼15 fuel-cup radii) such that propagation of boundary-induced disturbances into the region of interest is minimal. Flat velocity profiles are imposed at the fuel and air inflow boundaries, while an extrapolation procedure with weighted zeroth- and first-order terms is used to estimate the flow variables at the outflow boundary.

The outer diameter of the cup burner is 28 mm and the burner wall is treated as a 1-mm-long and 1-mm-thick tube. The wall temperature is set at 600 K. The inner diameter of the chimney is 95 mm. The mean fuel and oxidizer velocities are 0.921 and 10.7 cm/s, respectively. The low fuel velocity represents low-momentum conditions typical of condensed material fires. The air velocity is in the middle of the so-called "plateau region" [7,8,28], where the extinguishing agent concentration is independent of the oxidizer velocity.

The computed results are postprocessed to determine various variables. By assuming a stoichiometric expression for intermediate species in the mixture in which the elemental C and H are converted to CO_2 and H_2O, respectively, the local equivalence ratio (ϕ_{local}) is defined as

$$\sum_i X_i \left\{ (\mathrm{C}_n\mathrm{H}_m\mathrm{O}_l)_i + \left(n + \frac{m}{4} - \frac{l}{2}\right)\mathrm{O}_2 \right\} \rightarrow \sum_i X_i \left(n\mathrm{CO}_2 + \frac{m}{4}\mathrm{H}_2\mathrm{O} \right), \tag{2}$$

$$\phi_{\text{local}} = \frac{\sum_i X_i (n + m/4)}{\sum_i X_i (l/2)}. \tag{3}$$

Here, X_i denotes the mole fraction of species i. The mixture fraction was determined by the element mass fractions of carbon, hydrogen, and oxygen as defined by Bilger [39] as

$$\begin{aligned}\zeta = {} & \big((2/W_{\mathrm{C}})(Z_{\mathrm{C}} - Z_{\mathrm{C},2}) + (0.5/W_{\mathrm{H}})(Z_{\mathrm{H}} - Z_{\mathrm{H},2}) \\ & + (1/W_{\mathrm{O}})(Z_{\mathrm{O},2} - Z_{\mathrm{O}})\big) / \big((2/W_{\mathrm{C}})(Z_{\mathrm{C},1} - Z_{\mathrm{C},2}) \\ & + (0.5/W_{\mathrm{H}})(Z_{\mathrm{H},1} - Z_{\mathrm{H},2}) \\ & + (1/W_{\mathrm{O}})(Z_{\mathrm{O},2} - Z_{\mathrm{O},1})\big).\end{aligned} \tag{4}$$

At stoichiometry, the mixture fraction becomes

$$\begin{aligned}\zeta_{\mathrm{st}} = {} & \big((2/W_{\mathrm{C}})(-Z_{\mathrm{C},2}) + (0.5/W_{\mathrm{H}})(-Z_{\mathrm{H},2}) \\ & + (1/W_{\mathrm{O}})(Z_{\mathrm{O},2})\big) / \big((2/W_{\mathrm{C}})(Z_{\mathrm{C},1} - Z_{\mathrm{C},2}) \\ & + (0.5/W_{\mathrm{H}})(Z_{\mathrm{H},1} - Z_{\mathrm{H},2}) \\ & + (1/W_{\mathrm{O}})(Z_{\mathrm{O},2} - Z_{\mathrm{O},1})\big),\end{aligned} \tag{5}$$

where

$$\begin{aligned} Z_{\mathrm{C}} &= \sum_{i=1}^{N_{\mathrm{s}}} n_{\mathrm{C},i} \frac{W_{\mathrm{C}}}{W_i} Y_i, \\ Z_{\mathrm{H}} &= \sum_{i=1}^{N_{\mathrm{s}}} n_{\mathrm{H},i} \frac{W_{\mathrm{H}}}{W_i} Y_i, \\ Z_{\mathrm{O}} &= \sum_{i=1}^{N_{\mathrm{s}}} n_{\mathrm{O},i} \frac{W_{\mathrm{O}}}{W_i} Y_i. \end{aligned} \tag{6}$$

Hence, the subscripts 1 and 2 represent the fuel and air sides, respectively; $n_{\mathrm{C},i}$, $n_{\mathrm{H},i}$, and $n_{\mathrm{O},i}$ are the numbers of carbon, hydrogen, and oxygen atoms, respectively, in species i; W_i and Y_i are the molecular weight and mass fraction of species i; and N_{s} is the total number of species considered. The ϕ_{local} is identical to the conventional equivalence ratio in the unburned fuel–air mixture, and the ξ_{st} location is essentially identical to the $\phi_{\text{local}} = 1$ location.

4. Results and discussion

4.1. Visual observations

Fig. 2 shows video images of the cup-burner flame captured in microgravity aboard the KC-135 aircraft. Unlike the conical-shape flames in normal earth gravity [28] or elevated gravity (≈1.8g_{n}, not shown) during the aircraft pull-up period, the microgravity flame without agent (Fig. 2a) was fatter and much sootier. The blue flame zone was anchored at the outer edge of the burner rim and slightly inclined outward, in contrast to the inwardly inclined flames in 1g_{n}. The blue flame luminosity decreased downstream, while the yellow luminosity increased on the fuel side of the blue flame zone. As the agent (CO_2) was added stepwise into the air stream to a level lower than the extinguishing condition, the whole flame turned blue, it

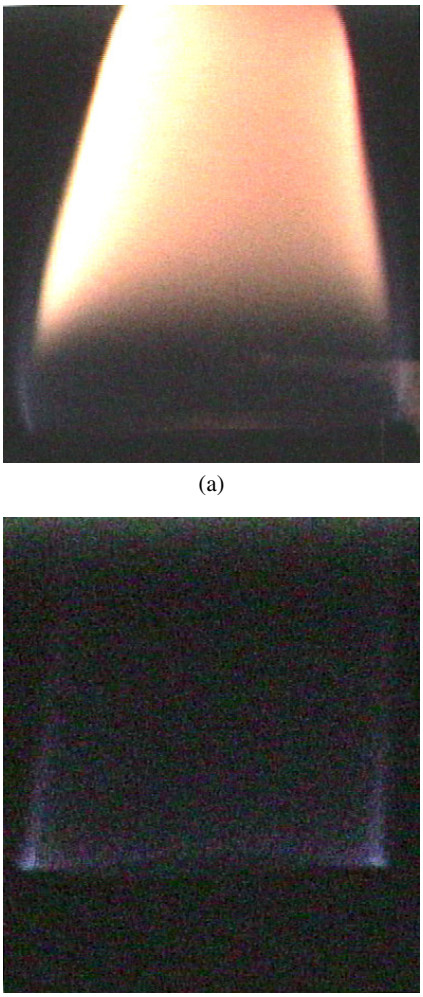

(a)

(b)

Fig. 2. Video images of microgravity methane diffusion flames in coflow air with or without added CO_2. Burner o.d.: 31 mm. $U_f = 0.9$ cm/s, $U_{ox} = 9.7$ cm/s. (a) No agent, (b) with 21.5% CO_2.

extended nearly parallel to the burner axis, and its tip opened. As the agent concentration was incrementally increased, the flame base detached from the burner rim and lifted gradually above the burner (Fig. 2b). The intensity of the blue flame zone showed a bright spot at the flame base and weakened downstream. As the flame base moved away farther downstream, the standoff distance from the burner fluctuated randomly up and down a few mm in response to the fluctuations in the velocity and concentration fields. The g-jitter influence generally observed in a quiescent μg environment appeared to be suppressed by the steady oxidizer flow in the present experiments. Eventually, the flame blew off and extinguished.

4.2. Extinguishing limits

Fig. 3 shows the measured ($X_{a,exp}$) critical agent (CO_2) volume fractions in the oxidizing flow at extinguishment as a function of the mean oxidizer velocity (U_{ox}) in μg together with the $1g_n$ data reported previously [28]. In $1g_n$, $X_{a,exp}$ was nearly independent over a wide range of U_{ox}, i.e., a plateau region [7,8,23]. In μg, the trend in $X_{a,exp}$ was similar (showing mild variation with U_{ox}), and for comparison purposes, the minimum extinguishing concentrations (MECs) of CO_2 (expressed as the volume fractions) were determined at an oxidizer velocity of $U_{ox} = 10.7$ cm/s (as used previously [28]). For the three conditions $1g_n$, μg with standard air ($X_{O_2,ox} = 0.21$ at 101 kPa), and μg with pre-EVA atmosphere ($X_{O_2,ox} = 0.3$ at 70.3 kPa), the MECs were 0.157, 0.237, and 0.440, respectively. The $X_{a,exp}$'s in the air at μg were approximately 1.5 times larger than those in $1g_n$, suggesting that cup-burner flames were more difficult to extinguish in μg. In $1g_n$, the inwardly directed upstream oxidizer flow contained vortices that caused oscillation of the flame base, which in turn blew off the flame [27,28]. On the other hand, in μg, because of the lack of buoyancy-induced oscillating-flow acceleration, the flame withstood the steady flow to higher $X_{a,exp}$ values before blowoff. In the oxygen-enriched pre-EVA μg environment, $X_{a,exp}$'s were approximately 1.8 times larger than those in air in μg. As will be described in detail later using the computational results, the higher oxygen concentration resulted in higher flame temperatures and required higher agent concentrations to cool off the flame to lead to blowoff. The high $X_{a,exp}$ values (>40%) suggest that fires in the pre-EVA μg environment would be very difficult to extinguish with CO_2 for both total-flooding and local applications.

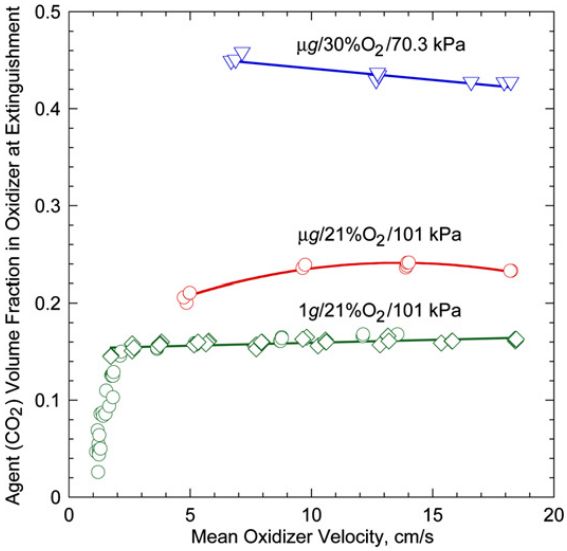

Fig. 3. Measured critical agent (CO_2) volume fractions in oxidizer at extinguishment for microgravity methane diffusion flames together with those in normal earth gravity measured previously [30] (points: experiments; lines: curve fits).

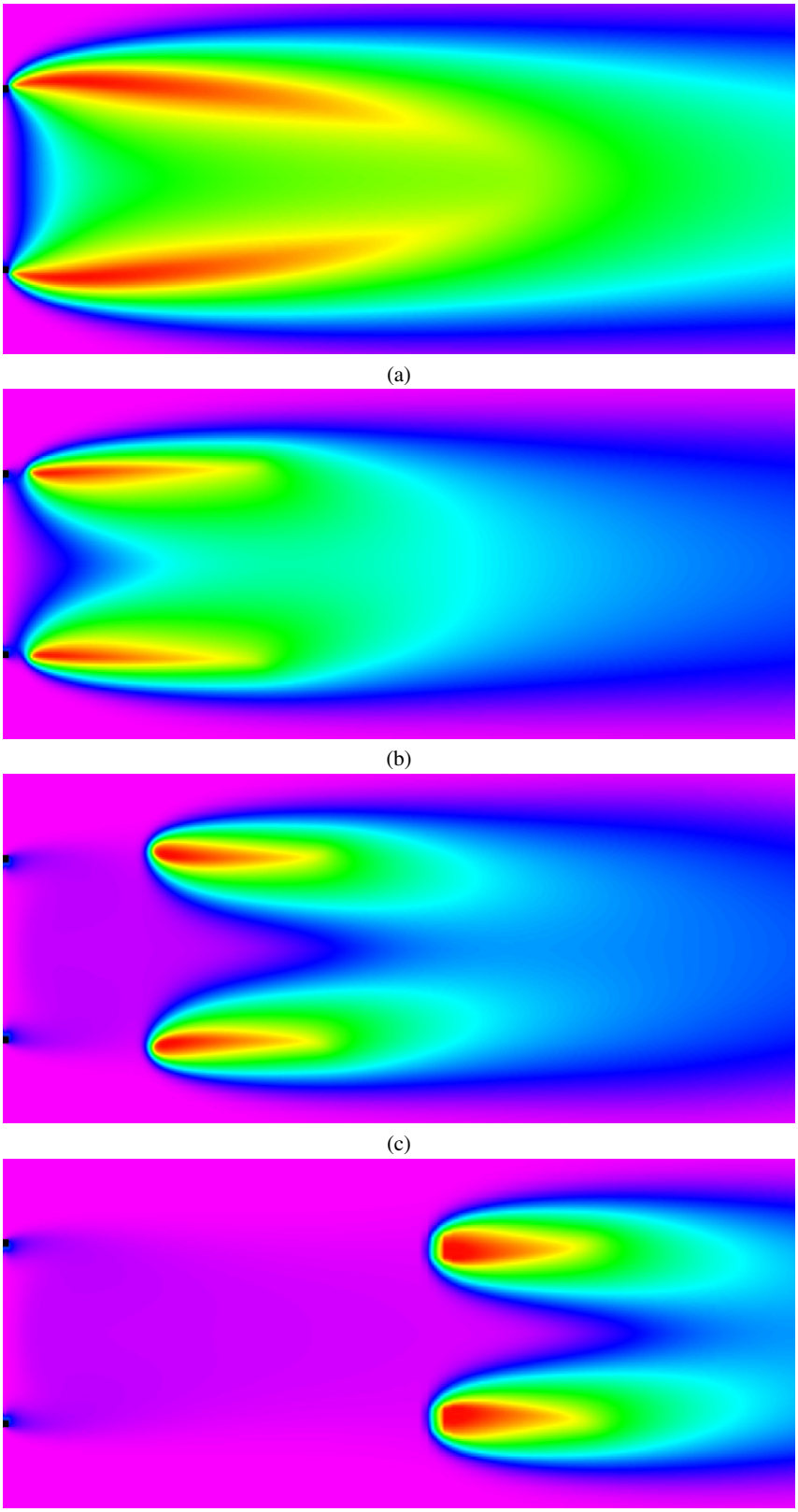

(a)

(b)

(c)

(d)

Fig. 4. Calculated ($C = 0.5$) temperature fields in $0g_n$ methane flames in air with or without added CO_2. $U_f = 0.92$ cm/s, $U_{ox} = 10.7$ cm/s. (a) No agent, $T_{max} = 1885$ K; (b) $X_a = 0.19$, $T_{max} = 1625$ K; (c) $X_a = 0.22$, $T_{max} = 1581$ K; (d) $X_a = 0.24$, $T_{max} = 1565$ K. Rainbow scale: 294 K (purple) to T_{max} (red).

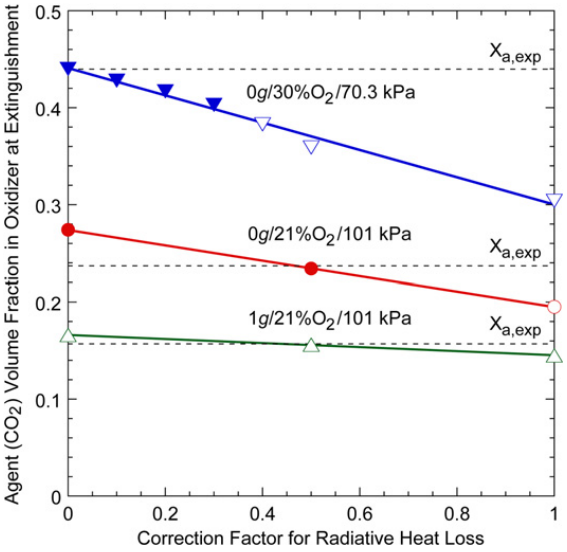

Fig. 5. Calculated critical agent (CO_2) volume fraction in oxidizer at extinguishment as a function of the correction factor for radiation in comparison with the measurement. $U_f = 0.92$ cm/s, $U_{ox} = 10.7$ cm/s.

Fig. 4 shows the calculated temperature fields in methane flames in air (Fig. 4a) and air with CO_2 (Figs. 4b to 4d) at various agent volume fractions (X_a's). A correction factor for radiation of $C = 0.5$ was used as described in the following paragraph. Without CO_2 addition (Fig. 4a), the maximum flame temperature (T_{max}) reached 1885 K. The temperature field showed the features of the fat attached flame experimentally observed (Fig. 2a). For $X_a = 0.19$ (Fig. 4b), the maximum flame temperature decreased 260 K, the flame base detached from the burner rim, and the flame tip cooled down and opened. With further CO_2 additions, the flame base lifted appreciably in parallel to the axis (Fig. 4c), as observed experimentally (Fig. 2b), and the flame base broadened laterally as it lifted off farther (Fig. 4d).

Fig. 5 shows the calculated ($X_{a,cal}$) critical agent (CO_2) volume fractions in the oxidizer as a function of the correction factor (C), together with the experimental values at $U_{ox} = 10.7$ cm/s (Fig. 3). In the computation, as X_a was increased incrementally (typically 0.001 near the limit), the flame either blew off rapidly from a relatively small standoff distance, or lifted off the burner continuously. In the latter case, the data points (filled symbols) were determined as the standoff distance exceeded 50 mm in order to maintain consistency and to avoid a coarser grid-spacing zone at a higher location. The effect of this arbitrarily chosen cutoff height on the $X_{a,cal}$ value determined was relatively small because the standoff distance was highly sensitive to X_a near the extinguishing limit as shown later. Although the calculated MECs ($X_{a,cal}$'s) of inert agents (N_2 and Ar) with $C = 1$ were in good agreement with the experiment in both $1g_n$ and μg (for both $X_{O_2,ox} = 0.21$ and 0.3) [28,29], $X_{a,cal}$'s of CO_2 in μg with $C = 1$ were substantially smaller than $X_{a,exp}$'s, particularly in the pre-EVA environment. The radiative heat transfer generally becomes more significant in μg than in $1g_n$ because the lack of buoyancy-induced flow acceleration results in longer residence times and lower heat-release rates. Although the radiative heat loss was included in the present computation, reabsorption was ignored (optically thin media were assumed). As a result, the radiative heat loss can be overestimated (for $C = 1$) if the radiating species are at high temperature and present at high concentrations.

In the pre-EVA μg-condition, the radiation loss term became particularly large because of the higher flame temperature and the higher CO_2 volume fraction at extinguishment, which makes the flame optically thicker. Thus, $X_{a,cal}$'s in μg matched better with $X_{a,exp}$'s using $C = 0.5$ for air and $C = 0$ for the pre-EVA environment. The correction factor of $C = 0$ suggested that the radiative heat loss balanced with the reabsorption (which was not considered in the present detailed computation). The correction factor used for air in this study ($C = 0.5$) was comparable to the value (0.54) reported previously [33] for solid fuel burning in an impinging air flow. Although the simplified radiation model with a correction factor has a lower level of complexity than the full-chemistry model used, the detailed flame structure and flow–transport–chemistry interactions obtained should provide useful insight into the complex blowoff processes.

4.3. Structure of the flame-stabilizing region

The inner structure of the flame base controls the flame attachment and detachment processes [18–21, 24–29]. Fig. 6 shows the calculated structure of a methane flame in air at $0g_n$ (with $C = 0.5$), including the velocity vectors ($\mathbf{v}$), isotherms (T), total heat-release rate ($\dot{q}$), and local equivalence ratio (ϕ_{local}) on the right and the total molar flux vectors of atomic hydrogen ($\mathbf{M}_H$), oxygen mole fraction (X_{O_2}), oxygen consumption rate ($-\hat{\omega}_{O_2}$), and mixture fraction (ξ), including stoichiometry ($\xi_{st} = 0.055$), on the left. The calculated flame base anchored at the outer edge of the burner rim, with a small quenched distance; the flame formed almost in parallel to the axis with some outward expansion in the near field and a slight inward inclination downstream. These qualitative features matched those of the observed blue flame zone (see Fig. 2a), although the downstream portion cannot be compared (due to obscuration by the luminous soot, which was not included in the computation).

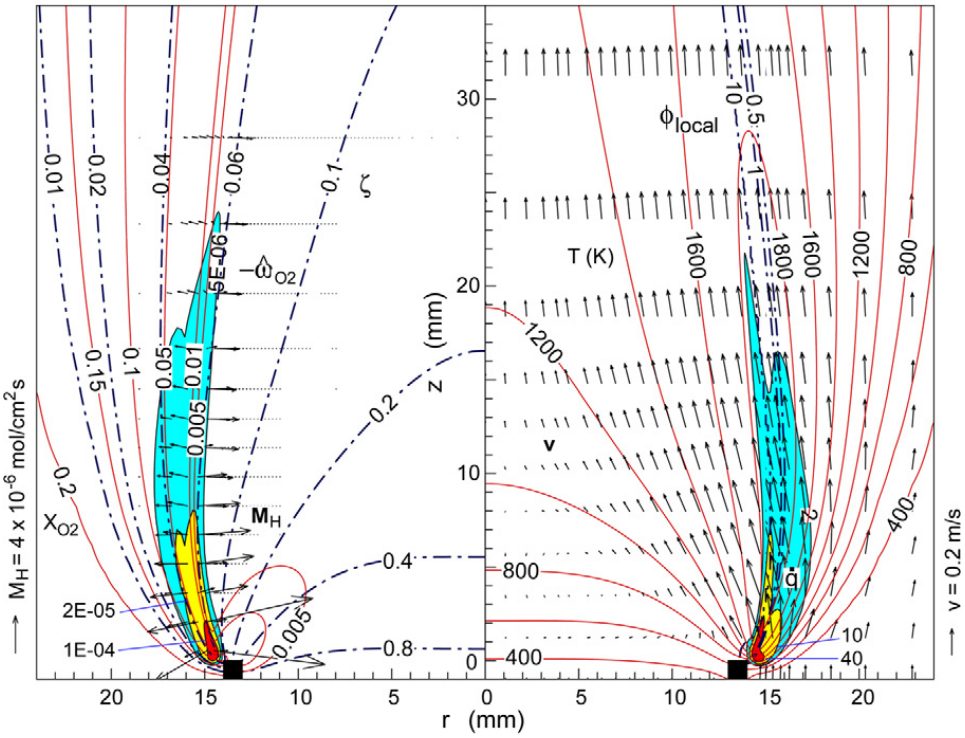

Fig. 6. Calculated structure ($C = 0.5$) of a $0g_n$ methane flame in air. $U_f = 0.92$ cm/s, $U_{ox} = 10.7$ cm/s. $\dot{q}$ contours (right): (2, 10, and 40) J/cm^3 s. $-\hat{\omega}_{O_2}$ contours (left): (5×10^{-6}, 2×10^{-5}, and 1×10^{-4}) mol/cm^3 s. $\zeta_{st} = 0.055$.

The velocity vectors show acceleration and streamtube expansion in the hot zone, particularly near the flame base, due to longitudinal and lateral thermal expansion of gases, respectively. Because of lack of buoyancy in $0g_n$, the acceleration was moderate as compared to the $1g_n$ case [22,23,28]. As the momentum and heat were transferred to the low-speed wake region behind the cup burner, the velocity distribution became more uniform downstream. The surrounding air came into the lower part of the flame, where the flame zone inclined outward. This trend resembled those of the jet diffusion flame formed on a smaller (3-mm i.d.) fuel tube in the coflowing (0.12 m/s) air in $0g_n$ previously studied (Fig. 6 in Ref. [19]).

The contours of both heat-release rate and oxygen-consumption rate showed a peak reactivity spot (the *reaction kernel* [18–21]) at the flame base. The chain radical species (H, OH, and O) diffused back against the incoming flow at the flame base (edge), where the oxygen concentration was relatively high compared to that in the trailing diffusion flame. Thus, the chain-branching ($H + O_2 \rightarrow O + OH$ [R73]) and subsequent reactions were enhanced, particularly at the flame base, thus forming the reaction kernel. The reactivity decreased steeply in downstream portions of the flame zone as this unique geometric feature of the edge diffusion flame was lost and the reactants were diluted by the combustion products, thus resulting in lower species concentration gradients and, in turn, fluxes. Thus, the reactivity nearly vanished downstream. Moreover, the flame temperature decreased downstream due to the low reactivity and radiative heat losses. Thus, the vigorously burning reaction kernel sustained stationary combustion processes in the flow in the vicinity of the burner rim (flame attachment) and held the trailing diffusion flame zone downstream, as described in detail elsewhere [18–21]. The heat-release rate, oxygen consumption rate, velocity, temperature, oxygen mole fraction, local equivalence ratio, and mixture fraction at the reaction kernel were $\dot{q}_k = 177$ J/cm^3 s, $-\hat{\omega}_{O_2,k} = 0.000488$ mol/cm^3 s, $|\mathbf{v}_k| = 0.313$ m/s, $T_k = 1478$ K, $X_{O_2,k} = 0.050$, $\phi_{local,k} = 0.61$, and $\xi_k = 0.048$, respectively.

Fig. 7 shows the variations of the species mole fractions (X_i), temperature, species formation rates ($\hat{\omega}_i$), and total heat-release rate across the reaction kernel of the undiluted $0g_n$ flame in air. Basic features in the flame structure are typical of diffusion flames: i.e., chain radicals, formed at high temperatures on the air side (slightly) of the peak reaction zone, diffuse and decompose the fuel into methyl, H_2, CO, and C_2 species (slightly) on the fuel side; finally, H_2 and CO are oxidized to the products on the air side. An exception is that due to the quenched space between the flame base and the burner rim (see also Fig. 6, X_{O_2} contours on the left side), the oxygen penetrated to the fuel side. The heat-release

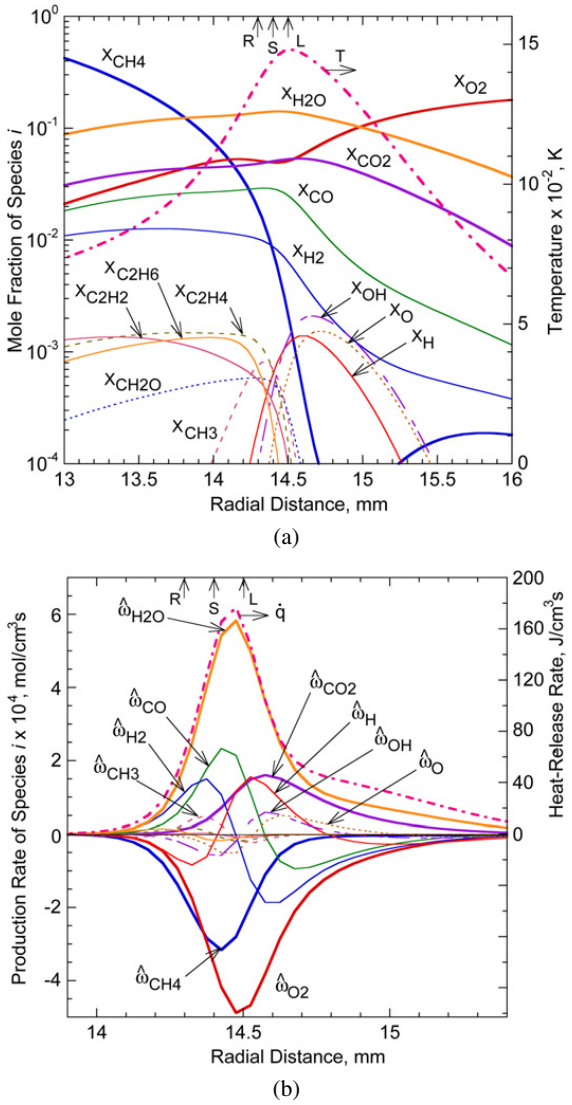

Fig. 7. Calculated structure ($C = 0.5$) at the reaction kernel height ($z_k = 0.33$ mm) for a $0g_n$ methane flame in air. Radial distributions of the (a) mole fractions, temperature, (b) species production rates, and total heat-release rate. S, L, and R: stoichiometric, lean, and rich flammability limits.

rates of elementary steps (not shown) revealed that the methyl oxidation reaction, $O + CH_3 \rightarrow H + CH_2O$ (R19), and the final product formation, $H_2 + OH \rightarrow H + H_2O$ (R165), were major contributors to the total heat-release rate peak. The reaction rates of elementary steps (not shown) indicated that the chain-branching, $H + O_2 \rightarrow O + OH$ (R73), was the fastest reaction of all, with its peak reaction rate coincident with the heat-release rate peak. Other fast reactions were the fuel dehydrogenation, $OH + CH_4 \rightarrow CH_3 + H_2O$ (R191) and $H + CH_4 \rightarrow CH_3 + H_2$ (R103), on the fuel side, the methyl oxidation (R19) at the heat-release rate peak, and the final product formation, (R165) and $OH + CO \rightarrow H + CO_2$ (R193) on the air side.

To determine the level of fuel–air mixing over the standoff distance and its effects on the internal structure of the reaction kernel, the radial distribution of the calculated local equivalence ratio ϕ_{local} (not shown) was analyzed. Fig. 7 also shows the radial locations at which the local equivalence ratios were at the stoichiometric condition (S), lower (L), and upper (U) flammability limits of the methane–air mixture; i.e., $\phi_{local} = 1, 0.53$, and 1.68, respectively (as converted from the methane concentrations in the literature [41]). Although ϕ_{local} is determined from the local composition of the reacting flow, it should reflect the condition of the incoming unburned gas mixture to produce the same composition because of the elemental mass conservation. The thickness of the layer within the flammability limits (0.2 mm) was an order of magnitude smaller than that of the reaction zone (≈1.5 mm), determined from the positive heat-release rate. Therefore, the reaction kernel existed under the fuel-lean (but not the fuel-rich) condition, and the air side of the reaction zone was below the lower flammability limit, i.e., super-lean conditions, burning as part of the diffusion flame structure. A triple (or tribrachial) flame structure [40] (i.e., the stoichiometric flame base with fuel-rich and fuel-lean premixed flame branches on the fuel and air sides, respectively) of lifted flames did not exist in the burner-rim-attached diffusion flame.

Changes in the flame structure near the base are profound, for even small variations in the CO_2 concentration near the extinguishing limit. Fig. 8 shows the calculated structure of near-limit flames in $0g_n$ (with $C = 0.5$) in air diluted with CO_2 at three different volume fractions in the oxidizer ($X_a = 0.19, 0.21$, and 0.22). As discussed later, the lean and rich flammability limits (expressed in terms of the equivalence ratio) are 0.74–1.19, 0.78–1.14, and 0.8–1.12 for $X_a = 0.19, 0.21$, and 0.22, respectively. These were determined from a flammability map presented by Coward and Jones for methane in air diluted with CO_2 [41].

For $X_a = 0.19$ (Fig. 8a), the flame base (with a standoff distance from the burner of 3.6 mm) supported the trailing diffusion flame in parallel to the axis. The oxygen leaked onto the fuel side of the flame zone, and the fuel–oxidizer mixing layer was formed. The mixing time (t_{mix}), determined by dividing the reaction kernel standoff distance by the mean oxidizer velocity ($U_{ox} = 10.7$ cm/s), was 43 ms. The flame zone cooled due to dilution and radiative heat losses. The values of the variables at the reaction kernel were $\dot{q}_k = 79$ J/cm^3 s, $-\hat{\omega}_{O_2,k} = 0.000217$ mol/cm^3 s, $|\mathbf{v}_k| = 0.163$ m/s, $T_k = 1423$ K, $X_{O_2,k} = 0.042$, $\phi_{local,k} = 0.60$, and $\xi_k = 0.036$.

For $X_a = 0.21$ (Fig. 8b), the flame base drifted downstream approximately 12 mm above the burner.

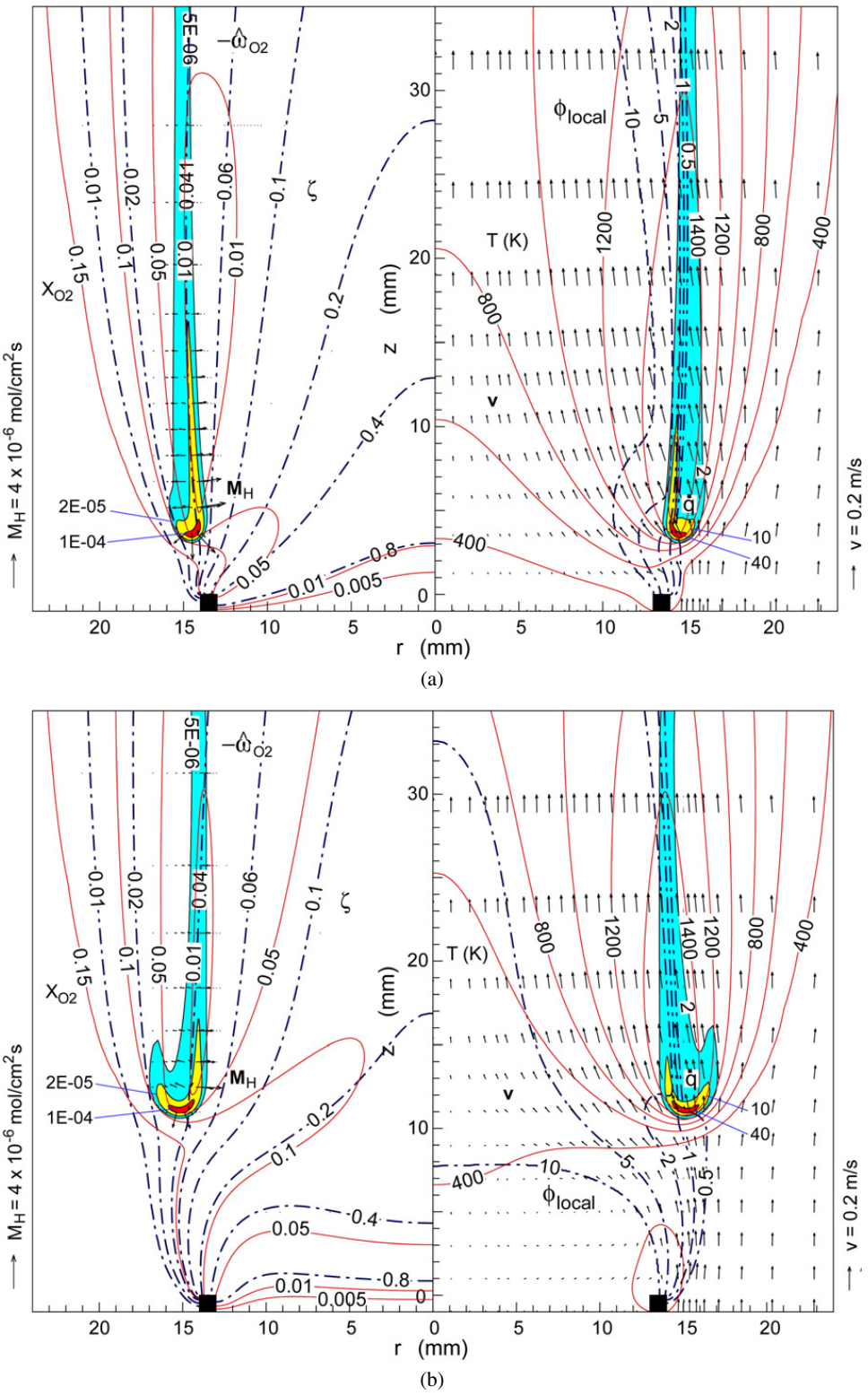

Fig. 8. Calculated structure ($C = 0.5$) of $0g_n$ methane flames in air with added CO_2. $U_f = 0.92$ cm/s, $U_{ox} = 10.7$ cm/s. $\dot{q}$ contours (right): (2, 10, and 40) J/cm^3 s. $-\hat{\omega}_{O_2}$ contours (left): (5×10^{-6}, 2×10^{-5}, and 1×10^{-4}) mol/cm^3 s. (a) $X_a = 0.19$, $\zeta_{st} = 0.041$; (b) $X_a = 0.21$, $\zeta_{st} = 0.040$; (c) $X_a = 0.22$, $\zeta_{st} = 0.039$.

The calculated reaction kernel location and the weak trailing diffusion flame were consistent with the visual observation of the bright spot at the flame base and the faint flame zone (Fig. 2b). The mixing time was $t_{mix} = 113$ ms. The values of the variables at the reaction kernel were $\dot{q}_k = 70$ J/cm^3 s,

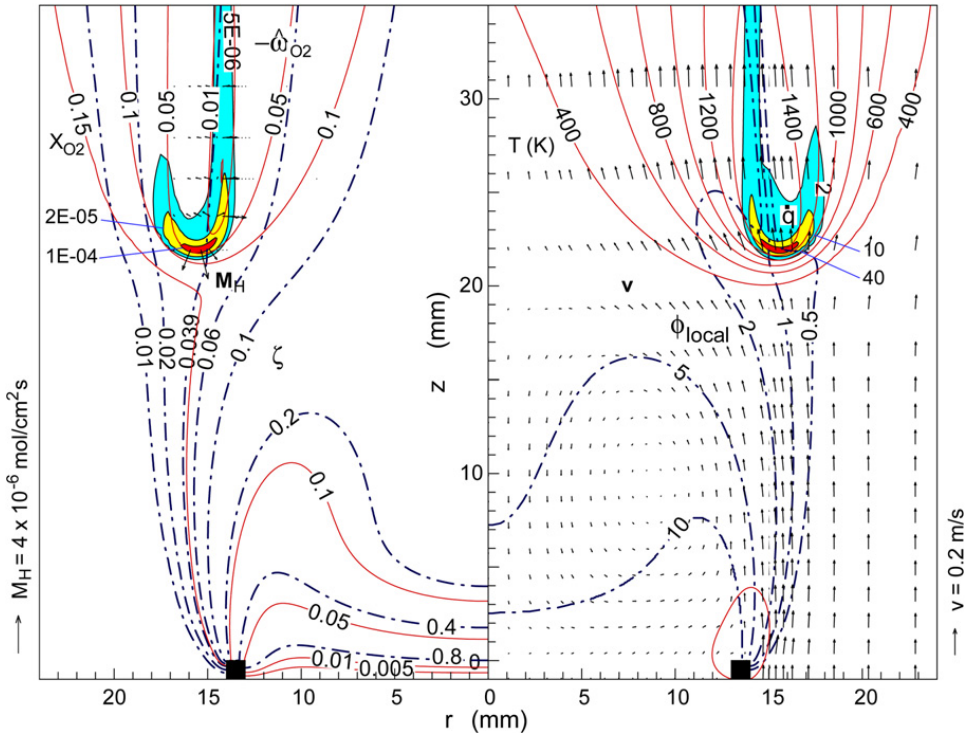

(c)

Fig. 8. (*continued*)

$-\hat{\omega}_{O_2,k} = 0.000186$ mol/cm^3 s, $|\mathbf{v}_k| = 0.163$ m/s, $T_k = 1424$ K, $X_{O_2,k} = 0.035$, $\phi_{local,k} = 0.78$, and $\xi_k = 0.037$.

For $X_a = 0.22$ (Fig. 8c), the flame base lifted farther downstream (23 mm), allowing more cold oxidizer to mix into the fuel side, and the recirculation zone in the wake of the cup burner became larger. As a result of the increased fuel–oxidizer mixing time ($t_{mix} = 214$ ms), the thickness of the flammable mixture layer increased. Consequently, the reaction kernel broadened laterally, thus forming a wing in the reactivity mapping on the air side. The values of the variables at the reaction kernel were $\dot{q}_k = 67$ J/cm^3 s, $-\hat{\omega}_{O_2,k} = 0.000168$ mol/cm^3 s, $|\mathbf{v}_k| = 0.169$ m/s, $T_k = 1418$ K, $X_{O_2,k} = 0.034$, $\phi_{local,k} = 0.76$, and $\xi_k = 0.036$. The reaction kernel extended far into the fuel-lean region.

Fig. 9 shows the radial and axial variations of calculated variables crossing the reaction kernel of the flame at $X_a = 0.19$ shown in Fig. 8a. As a result of increased flame–base standoff distance, oxygen penetrated onto the fuel side and methane leaked out onto the oxidizer side, thus promoting fuel–oxidizer mixing. As the reaction kernel burns against the incoming flow, the methane and oxygen mole-fraction distributions show dips; however, the radial thickness of the layer within the flammability limits remained thin (≈0.2 mm) compared to that of the reaction zone (≈2 mm). As the CO_2 mole fraction more than quadrupled over the reaction zone compared to the undiluted flame (Fig. 7) (e.g., from $X_{CO_2} = 0.053$ to 0.221 at $r = 14.6$ mm), the level of the H_2 concentration dropped and that of CO increased, probably because of an equilibrium in the water gas shift reactions: $CO + H_2O \leftrightarrow CO_2 + H_2$. This result demonstrates the chemical effect of CO_2 addition, besides the thermal effect. The axial distributions of the calculated variables crossing the reaction kernel (Figs. 9c and 9d) showed some premixed nature of the structure; i.e., the fuel and oxygen mole fractions decreased, while the temperature increased and the heat-release rate peaked at the reaction kernel. The axial thickness of the reaction zone, defined as the full width at the half height (FWHH) of the heat-release rate peak, was ≈0.4 mm.

For $X_a = 0.22$ (Fig. 10), the increased mixing time changed the flame structure significantly. The dips in the methane and oxygen mole-fraction distributions expanded, thus forming a unique mirrored flame structure (Fig. 10a) as the reaction zone (defined as the region of positive heat release) broadened radially (≈3 mm) (Fig. 10b). The radial thickness of the flammable layer (≈0.4 mm) became comparable to the axial FWHH of the heat-release rate peak (≈0.4 mm), which remained unchanged (Fig. 10d). As the reaction kernel drifted downstream and the mixing progressed ($z_k \approx 22$ mm, $t_{mix} = 214$ ms), the premixed combustion wave structure was getting

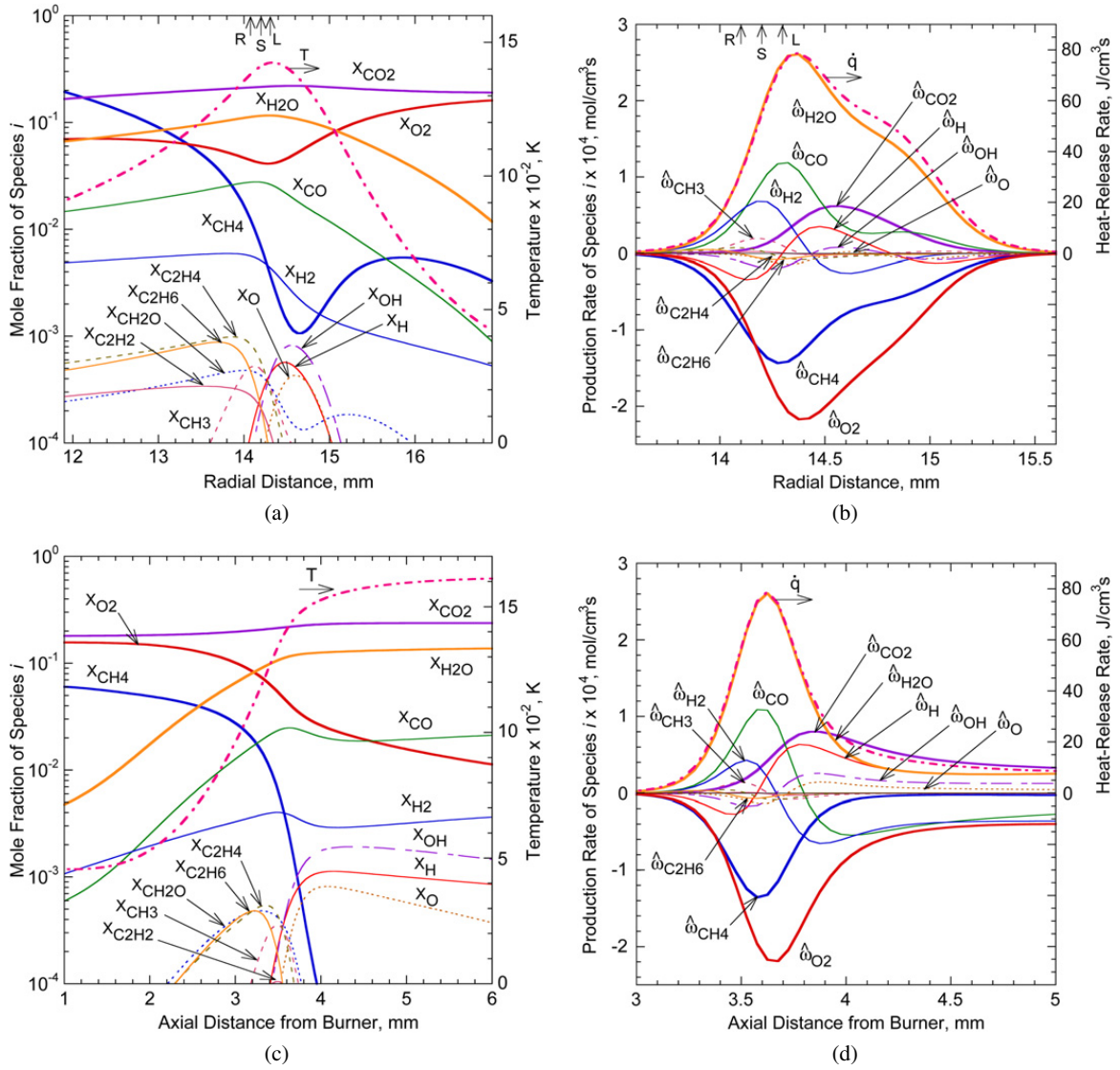

Fig. 9. Calculated structure ($C = 0.5$) through the reaction kernel for a $0g_n$ methane flame in air with added CO_2 ($X_a = 0.19$, $z_k = 3.6$ mm, $r_k = 14.4$ mm). (a), (b) Radial and (c), (d) axial variations of the (a), (c) mole fractions, temperature; (b), (d) species production rates, and total heat-release rate. S, L, and R: stoichiometric, lean, and rich flammability limits.

formed. Nonetheless, the wing in the reactivity on the air side (Fig. 8c) was still below the lean flammability limit, under which condition the ordinary premixed flame would not possess a laminar flame speed, i.e., an ability to propagate against the flow. On the air side, the $H + O_2 + M \rightarrow HO_2 + M$ (R65) and subsequent $OH + HO_2 \rightarrow O_2 + H_2O$ (R171) reactions with null activation energy were very exothermic even at relatively low temperatures and thus contributed to the total heat release. The fuel-lean reaction kernel maintained stationary burning, thus supporting the super-lean wing on the air side as well as the trailing diffusion flame zone on the fuel-rich side. Furthermore, because the flammable mixture layer was so thin (radially), the triple flame structure with the fuel-lean and fuel-rich premixed flame branches was not formed. In a previous paper [27], computations of the edge diffusion flame propagation through a flammable mixture layer, with a sufficiently long mixing time (0.3 s), using a detailed reaction mechanism revealed that C_1 to C_3 alkanes did not form the triple flame structure, whereas ethylene and acetylene did. The rich flammability limit and the chemical pathway were responsible for the different fuel-dependent behavior. Moreover, the one-step chemistry without artificial flammability-limit boundaries may lead to unrealistic results, as demonstrated previously [18].

4.4. *Flame-tip extinction and blowoff extinguishment processes*

Unlike in $1g_n$, in which buoyancy-induced flow acceleration causes severe flame base oscillation and

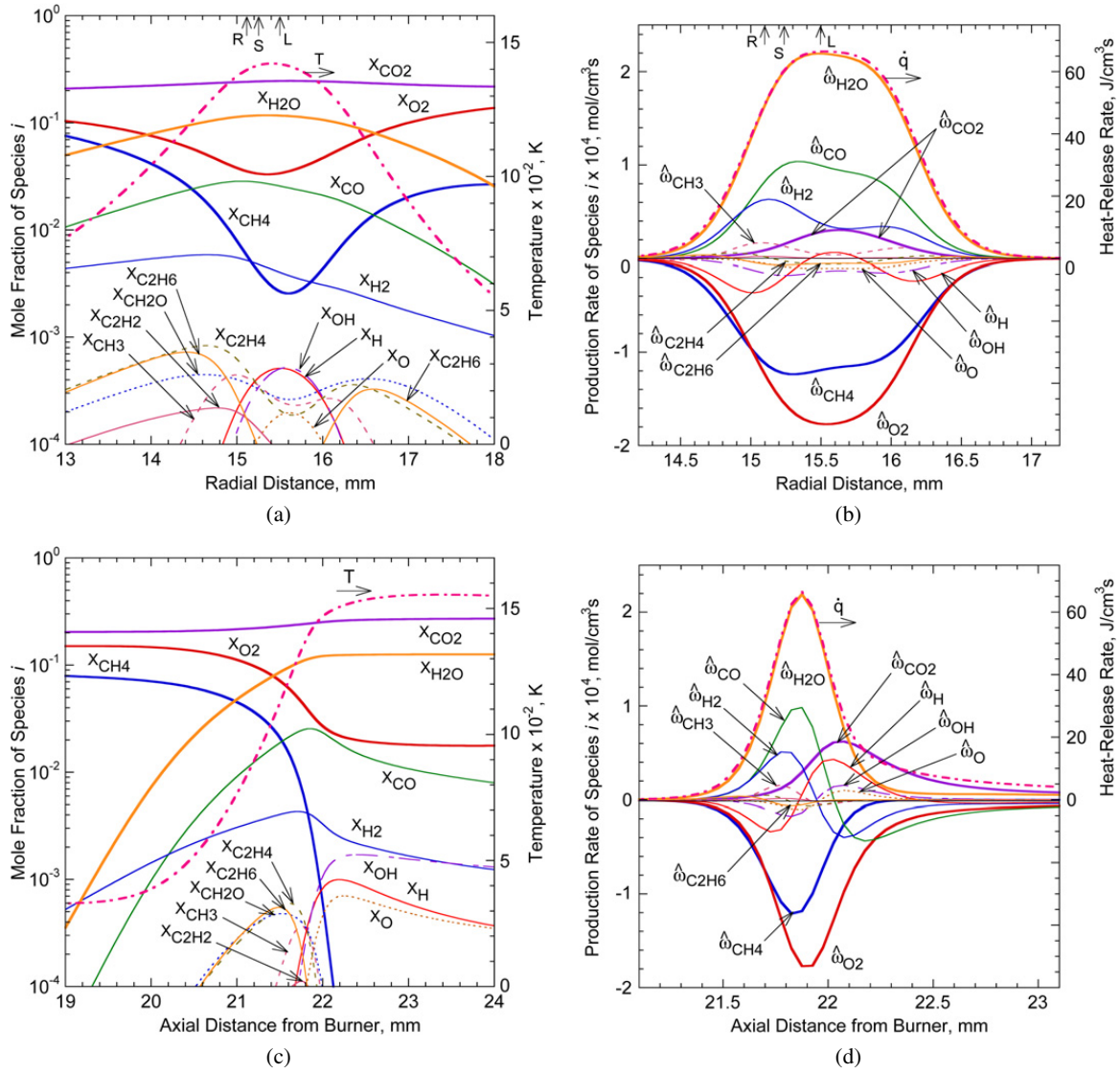

Fig. 10. Calculated structure ($C = 0.5$) through the reaction kernel for a $0g_n$ methane flame in air with added CO_2 ($X_a = 0.22$, $z_k = 21.9$ mm, $r_k = 15.5$ mm). (a), (b) Radial and (c), (d) axial variations of the (a), (c) mole fractions, temperature; (b), (d) species production rates, and total heat-release rate. S, L, and R: stoichiometric, lean, and rich flammability limits.

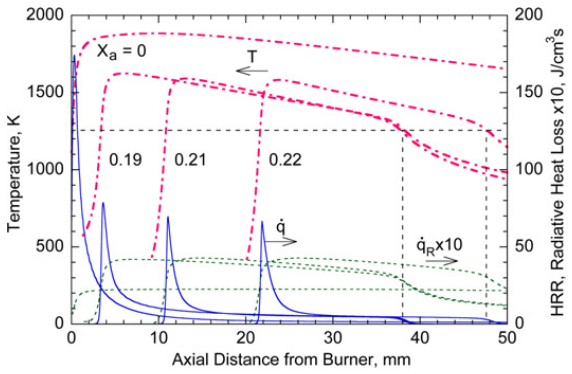

Fig. 11. Calculated ($C = 0.5$) temperature, heat-release rate, and radiative heat losses along the flame zone in $0g_n$ methane flames in air with or without added CO_2.

subsequent self-blowoff [27,28], the cup-burner flame extinguishment in μg took place more gradually. Fig. 11 shows the calculated temperature, heat-release rate, and radiative heat losses ($\dot{q}_R$) along the flame zone (defined as the radial maximum T envelope for T and the $\dot{q}$ evelope for $\dot{q}$ and $\dot{q}_R$) for various agent (CO_2) volume fractions in the oxidizer. In the undiluted flame ($X_a = 0$), the temperature reached a maximum of 1885 K around $z = 10$ mm and decreased linearly downstream due to radiative heat losses at a rate between those for the cases with $C = 0$ and 1 previously reported [23]. The heat-release rate showed a peak ($\dot{q}_k = 174$ J/cm^3 s at $z_k = 0.33$ mm, as shown in Fig. 6), decreased sharply downstream, and was maintained at low levels until vanishing at the flame tip on the centerline around $z = 80$ mm.

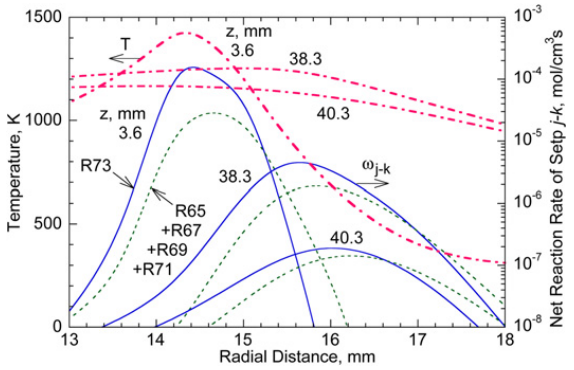

Fig. 12. Calculated ($C = 0.5$) temperature and the net reaction rates of chain branching (R73) and chain breaking (R65 through R71) reactions at three heights (the reaction kernel, flame tip, and 2-mm downstream) in a $0g_n$ methane flame in air with added CO_2 ($X_a = 0.19$).

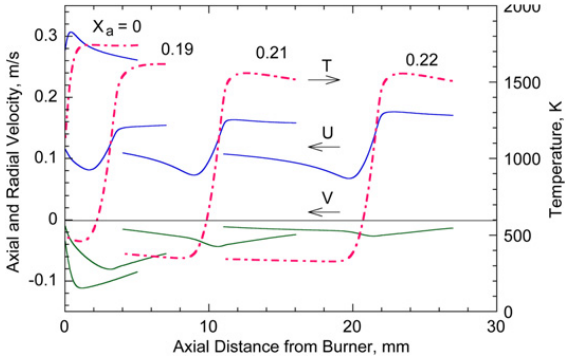

Fig. 13. Axial variations of the calculated ($C = 0.5$) axial and radial velocity components and temperature crossing the reaction kernel of $0g_n$ methane flames in air with added CO_2.

For $X_a = 0.19$, the maximum temperature and heat-release rate decreased to 1625 K and $\dot{q}_k = 81\ \mathrm{J/cm^3\,s}$, respectively. As a result of increased CO_2 concentration, the radiative heat loss nearly doubled, and the slope of the flame temperature profile increased. For all flames with the CO_2 addition, the temperature decreased smoothly downstream to ≈1300 K, at which point both the heat-release rate and the temperature dropped more rapidly. Eventually, the heat-release rate equals the heat loss ($\dot{q} = \dot{q}_R \approx 3\ \mathrm{J/cm^3\,s}$) at $T \approx 1255$ K (see dashed lines), thereby shutting off exothermic reactions. Thus, the flame tip opened as local extinction occurred downstream. As X_a was increased, the length at which this local extinction occurred (i.e., the flame length) became less.

Asymptotic analyses of flames [42,43] emphasize the importance of the inner layer temperature on flame extinction. This temperature corresponds in diffusion flames to the radial maximum temperature reported here. It has been postulated that if that temperature approaches the crossover temperature between chain branching and chain breaking, extinction occurs. To see if this argument applies to the present flame-tip extinction, the calculated reaction rates were examined. Fig. 12 shows the variations of the temperature and the net (forward minus backward) reaction rates of chain-branching ($H + O_2 \rightarrow O + OH$ [R73]) and the sum of chain-breaking reactions ($H + O_2 + M \rightarrow HO_2 + M$ [R65], $H + O_2 + O_2 \rightarrow HO_2 + O_2$ [R67], $H + O_2 + H_2O \rightarrow HO_2 + H_2O$ [R69], $H + O_2 + N_2 \rightarrow HO_2 + N_2$ [R71]) crossing the flame at three heights: the reaction kernel ($z = 3.6$ mm), the $\dot{q} = \dot{q}_R$ point ($z = 38.3$ mm), and 2 mm downstream ($z = 40.3$ mm). The rate of chain branching was larger than that of chain breaking at the reaction kernel, obviously, and even at the flame tip ($\dot{q} = \dot{q}_R$ at $T \approx 1255$ K). The crossover occurred on the air side at all three heights at a lower temperature of ≈1100 K. Therefore, the flame tip extinction occurred before the radial maximum temperature decreased to the crossover temperature.

Fig. 13 shows the variations of the temperature and velocity components crossing the reaction kernel parallel to the z-axis. The temperature rises steeply as the flame base is approached and then drops slowly as described above. With added CO_2, the axial velocity (U) first decreases toward the flame base (due to stream-tube expansion into the wake region behind the low velocity fuel jet as well the streamline deflection around the flame base, as shown in Fig. 8) and then increases downstream as a result of longitudinal gas expansion due to temperature rise. As X_a was increased (from 0.19 to 0.22), the absolute values of the radial component decreased to null (the incoming flow became parallel to the axis). The minimum axial velocity component just before the temperature rise (i.e., the apparent flame speed) was ≈0.07 m/s at $X_a = 0.22$.

Fig. 14 shows the effects of the agent volume fraction in the oxidizer on the calculated reaction kernel properties: the axial (z_k) and radial (r_k) positions from the burner exit on the axis (Fig. 14a) and the total ($|\mathbf{v}_k|$), axial (U_k), and radial velocity (V_k) (Fig. 14b). (Values are shown for μg conditions, with $X_{O_2,ox} =$ 0.21 or 0.30 and the corresponding total pressure.) As X_a was increased, the axial standoff distance of the reaction kernel increased gradually and then more steeply as the extinguishing limit approached. For each X_a, a steady-state solution for a stable stationary flame was obtained. The radial location of the reaction kernel remained nearly constant, while the flame base was close to the burner rim, and decreased slightly as it detached, and increased as it lifted off. The absolute values of $|\mathbf{v}_k|$, U_k, and V_k decreased (i.e., the residence time through the reaction kernel

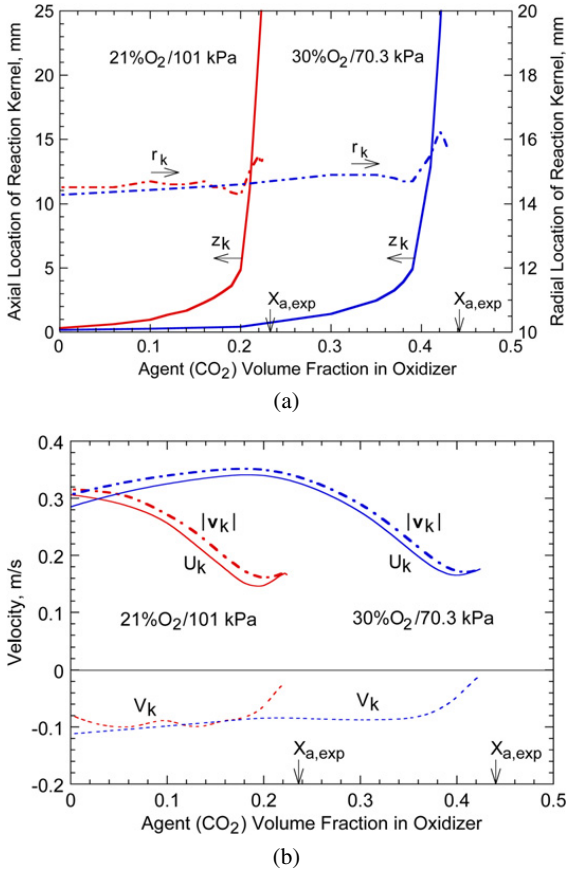

Fig. 14. Calculated reaction kernel properties with added CO_2 in oxidizer stream of a $0g_n$ methane flame: (a) reaction kernel coordinates and (b) axial and radial velocity components and total velocity. ($C = 0.5$ for $X_{O_2,ox} = 0.21$ and $C = 0$ for $X_{O_2,ox} = 0.3$.)

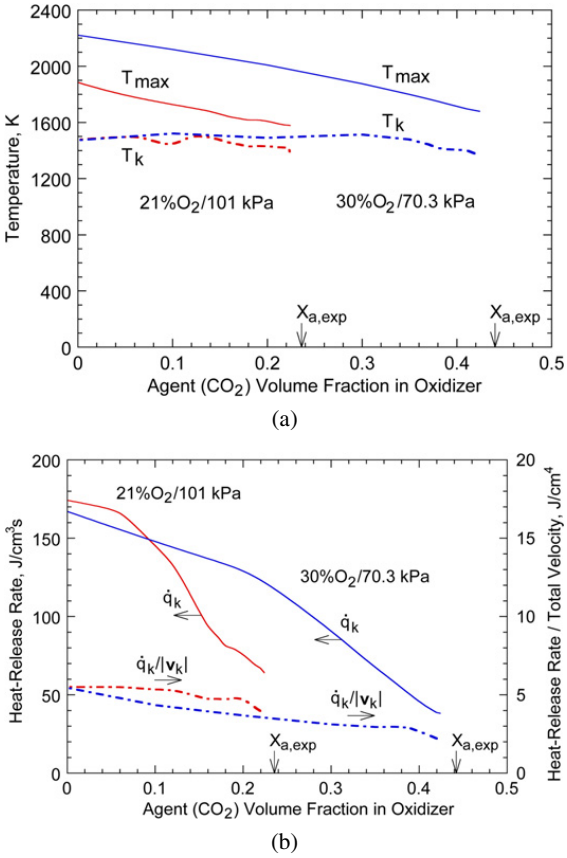

Fig. 15. Calculated flame structure of a $0g_n$ methane flame with added CO_2 in oxidizer stream: (a) maximum trailing flame and reaction kernel temperatures and (b) heat-release rate and its ratio to total velocity at the reaction kernel ($C = 0.5$ for $X_{O_2,ox} = 0.21$ and $C = 0$ for $X_{O_2,ox} = 0.3$).

increased) generally with increasing X_a, except for initial increases in $|\mathbf{v}_k|$ and U_k for $X_{O_2,ox} = 0.3$.

Fig. 15 shows the maximum temperature in the trailing diffusion flame, the reaction kernel temperature (Fig. 15a), the heat-release rate, and a ratio of the heat-release rate and the total velocity (Fig. 15b). The maximum flame temperatures for $X_{O_2,ox} = 0.21$ and 0.3 without agent were 1885 and 2222 K, respectively, and decreased with increasing X_a linearly down to a range of 1600 to 1700 K. Thus, the $X_{O_2,ox} = 0.3$ case needed more agent to cool the flame zone to this level. On the other hand, the reaction kernel temperature was fairly constant within a range of 1400 to 1500 K, for both cases. The heat-release rate decreased with increasing X_a, and thus, the flame stabilized at a location that provided a larger reaction time. The quantity $\dot{q}_k/|\mathbf{v}_k|$ (which relates to the ratio of the residence time and the reaction time, i.e., local Damkhöler number, at the reaction kernel [18]) decreased mildly over a wide range and more rapidly as the flame lifted off the burner. This result suggests that the reaction kernel shifted downstream to seek a location where longer residence time is available for longer reaction time caused by CO_2 addition (which lowers the overall reaction rate). A subtle balance between the residence time and the reaction time must be important in flame stabilization as proposed previously for jet diffusion flames in which the coflow air velocity was increased (decreasing the residence time) [18].

5. Conclusions

The reduced-gravity aircraft experiments and numerical simulations with full chemistry have revealed the flame structure and blowoff mechanisms of methane–air coflow diffusion flames in the cup-burner configuration. Absence of gravity uncovered the essential flame stabilization processes without complications of the flame–base oscillation and self-blowoff phenomena encountered in $1g_n$. The peak-reactivity spot (reaction kernel) at the flame base is responsible for both the trailing diffusion flame holding and extinguishment. In $0g_n$, the attached flame

zone was formed in parallel to the axis due to lack of buoyancy-induced flow acceleration. The flame tip opened due to local extinction by radiative heat losses when the calculated local flame temperature decreased below ≈1300 K. Addition of CO_2 to the oxidizer decreased the maximum trailing flame temperature toward a threshold value (≈1600 K) and weakened the reaction kernel, thereby inducing the flame–base detachment and blowoff-type extinguishment. At the reaction kernel height, the thickness of the layer that was within the flammability limits was an order of magnitude thinner than that of the reaction zone (i.e., the region of positive heat release) and the oxidizer-side reactivity branch of lifted flame base existed under the super-lean conditions (i.e., beyond the ordinary premixed flammability limits).

Acknowledgments

This research was supported by the Office of Biological and Physical Research and the Fire Prevention, Detection, and Suppression Program in the Exploration Technology Development Program Office, National Aeronautics and Space Agency, Washington, DC. Assistance by Philip Werk, Benjamin Chan, Jeffrey Taggart (Case Western Reserve University), David Bennett (Jacobs Sverdrup), Mike Jamison (ZIN Technologies), Gary Ruff, James Withlow, and John Yaniec (NASA) in conducting the experiment is acknowledged.

References

[1] R. Friedman, Fire safety in extraterrestrial environments, NASA/TM-1998-207417, 1998.
[2] R. Friedman, Fire safety in the low-gravity spacecraft environment, NASA/TM-1999-209285, 1999.
[3] R. Friedman, H.D. Ross, in: H.D. Ross (Ed.), Microgravity Combustion: Fire in Free Fall, Academic Press, San Diego, 2001, p. 83.
[4] Anon., Report of the Halon Fire Extinguishing Agents Technical Options Committee, United Nations Environment Programme (UNEP), 1994.
[5] J. Opfell, Fire detection and fire suppression trade study, Report No. 85-22472, Rev. 1 AirResearch Los Angeles Division, Allied-Signal Aerospace Company, 1985.
[6] J.G. Shridan, A systems analysis of fire suppression alternatives for the U.S. Space station, MS thesis, AFIT/GSO/AA/37D-5, Air Force Institute of Technology, 1987.
[7] A. Hamins, G. Gmurczyk, W. Grosshandler, R.G. Rehwoldt, I. Vazquez, T. Cleary, C. Presser, K. Seshadri, in: W.L. Grosshandler, R.G. Gann, W.M. Pitts (Eds.), Evaluation of Alternative In-Flight Fire Suppressants for Full-Scale Testing in Simulated Aircraft Engine Nacelles and Dry Bays, NIST SP 861, National Institute of Standards and Technology, Gaithersburg, MD, 1994, pp. 345–465.
[8] T.A. Moore, A. Martinez, R.E. Tapscott, in: 7th Halon Options Technical Working Conference (HOTWC-97), Albuquerque, NM, 1997, pp. 388–395.
[9] R.T. Wickham, Review of the use of carbon dioxide total flooding fire extinguishing systems, 2003. Available at: http://www.epa.gov/Ozone/snap/fire/index.html.
[10] Anon., Standard on carbon dioxide extinguishing systems, NFPA 12, 2005 Edition National Fire Protection Association, Quincy, MA, 2005.
[11] Anon., Workshop on research for space exploration: Physical sciences and process technology, NASA/CP-1998-207431, 1998.
[12] J.W. Brown, J. Kosmo, P.D. Campbell, Internal atmospheric pressure and composition for planet surface habitats and extravehicular mobility units, NASA JSC-25003, LESC-29278, 1991.
[13] C.E. Martin, R.C. DaLee, Spacecraft fire detection and suppression (FDS) systems: An overview and recommendations for future flights, in: 23rd International Conference on Environmental Systems, Colorado Springs, CO, SAE 932166, 1993.
[14] R. Friedman, Independent assessment of the proposed fire detection and suppression subsystem for the space station freedom, NASA Lewis Research Center, 1993.
[15] K.E. Lange, A.T. Perka, B.E. Duffield, F.F. Jeng, Bounding the spacecraft atmosphere design space for future exploration missions, NASA/CR-2005-213689, 2005.
[16] L. Qiao, Y. Gu, W.J.A. Dahm, E.S. Oran, G.M. Faeth, Proc. Combust. Inst. 31 (2007) 2701–2709.
[17] K.M. Shebl, A.M. Abdilghanie, W.J.A. Dahm, G.M. Faeth, Extinction of opposed-flow hydrocarbon diffusion flames by chemically-passive suppressants at normal and EVA atmosphere conditions, AIAA Paper 2006-0740, 2006.
[18] F. Takahashi, V.R. Katta, Proc. Combust. Inst. 28 (2000) 2071–2078.
[19] F. Takahashi, V.R. Katta, Proc. Combust. Inst. 29 (2002) 2509–2518.
[20] F. Takahashi, V.R. Katta, Proc. Combust. Inst. 30 (2005) 383–390.
[21] F. Takahashi, V.R. Katta, Proc. Combust. Inst. 30 (2005) 375–382.
[22] V.R. Katta, F. Takahashi, G.T. Linteris, in: D.D. Evans (Ed.), Fire Safety Science: Proceedings of the Seventh International Symposium, International Association for Fire Safety Science, London, 2003, pp. 531–542.
[23] V.R. Katta, F. Takahashi, G.T. Linteris, Combust. Flame 137 (2004) 506–522.
[24] G.T. Linteris, V.R. Katta, F. Takahashi, Combust. Flame 138 (2004) 78–96.
[25] V.R. Katta, F. Takahashi, G.T. Linteris, Combust. Flame 144 (2005) 645–661.
[26] G.T. Linteris, F. Takahashi, V.R. Katta, Combust. Flame 149 (2007) 91–103.
[27] F. Takahashi, G.T. Linteris, V.R. Katta, Proc. Combust. Inst. 31 (2007) 1575–1582.

[28] F. Takahashi, G.T. Linteris, V.R. Katta, Proc. Combust. Inst. 31 (2007) 2721–2729.
[29] F. Takahashi, G.T. Linteris, V.R. Katta, Combustion and extinguishment characteristics of cup-burner flames, Central States Section Meeting, The Combustion Institute, Pittsburgh, PA, 2006.
[30] Anon., Standard on clean agent fire extinguishing systems, NFPA 2001, National Fire Protection Association, Quincy, MA, 2000.
[31] Anon., Gaseous fire-extinguishing systems—Physical properties and system design, ISO 14520-Part I, International Organization for Standardization, 2000.
[32] H. Bedir, J.S. T'ien, H.S. Lee, Combust. Theory Model. 1 (1997) 395–404.
[33] J.L. Rhatigan, H. Bedir, J.S. T'ien, Combust. Flame 112 (1998) 231–241.
[34] V.R. Katta, L.P. Goss, W.M. Roquemore, AIAA J. 32 (1) (1994) 84–94.
[35] W.M. Roquemore, V.R. Katta, J. Visualization 2 (3/4) (2000) 257–272.
[36] M. Frenklach, H. Wang, M. Goldenberg, G.P. Smith, D.M. Golden, C.T. Bowman, R.K. Hanson, W.C. Gardiner, V. Lissianski, GRI-Mech—An optimized detailed chemical reaction mechanism for methane combustion, Report No. GRI-95/0058, Gas Research Institute, Chicago, IL, 1995.
[37] J.O. Hirschfelder, C.F. Curtis, R.B. Bird, The Molecular Theory of Gases and Liquids, Wiley, New York, 1954.
[38] R.S. Barlow, A.N. Karpetis, J.H. Frank, J.-Y. Chen, Combust. Flame 127 (2001) 2102–2118.
[39] R.W. Bilger, Proc. Combust. Inst. 22 (1988) 475–488.
[40] S.H. Chung, Proc. Combust. Inst. 31 (2007) 877–892.
[41] B. Lewis, G. von Elbe, Combustion, Flames and Explosions of Gases, third ed., Academic Press, Orlando, FL, 1987.
[42] K. Seshadri, N. Peters, Combust. Flame 73 (1988) 23–44.
[43] K. Seshadri, Proc. Combust. Inst. 26 (1996) 831–846.